Carbon 205 (2023) 180–193

Contents lists available at ScienceDirect

Carbon

journal homepage: www.elsevier.com/locate/carbon

Surface morphology and carbon structure effects on sputtering: Bridging scales between molecular dynamics simulations and experiments

H. Tran, H.B. Chew *

Department of Aerospace Engineering, University of Illinois at Urbana-Champaign, Urbana, IL 61801, USA

ARTICLE INFO

Keywords:
Carbon sputtering
Noble gas ions
Surface morphology
Plasma-material interaction
Molecular dynamics

ABSTRACT

Experiments report large scatter in the sputtering yield of carbon materials under the bombardment of low-energy noble gas ions. Here, we conduct scale-bridging molecular dynamics (MD) simulations on the xenon bombardment of carbon substrates across ion energies of 75 eV to 2 keV, and at ion incidence angles of 0°–75°, to resolve uncertainties in the sputtering data. Results show rapid amorphization of the carbon subsurface with ion bombardment, but the structural characteristics ($sp/sp^2/sp^3$ bond proportion, atomic density) eventually plateau once steady-state sputtering is achieved. In addition, we obtain virtually indistinguishable "steady-state" amorphous structures across the range of ion energies and ion incidence angles, as well as for several different carbon structures, which suggests that the steady-state sputtering yield data is independent of the initial carbon structure and prior sputtering history. By accounting for changes in the local incidence angle, surface shielding, and redeposition of the sputterants associated with surface morphology effects, we demonstrate that the sputtering predictions from MD are in perfect agreement with prior experiments across the range of ion energies and incidence angles. Using a Bayesian approach based on the MD data, we calibrate the parameters of a semi-empirical sputtering model for different surface morphologies.

1. Introduction

Sputtering is a physical phenomenon describing the ejection of particles from a surface by the bombardment of energetic ions. This process allows for controlled removal of surface layers [1,2], patterning of surfaces [3], and even the etching of holes with sub-micrometer resolution [4–8]. In other applications, the removed materials from sputtering are deposited as film coatings on a wide variety of substrates to enhance their physical, mechanical, and optical properties [9–12]. In many plasma-surface interactions, however, sputtering is not desirable since it erodes the material and alters the plasma operational conditions [13–15]. One important example is the gridded ion thrusters in electric space propulsion systems, where the impingement of charge-exchange xenon ions on the inside of the accelerator grid holes widens these holes during operation [16]. To extend the thruster life, the grid material is often fabricated from graphite, because of its low sputter yield and low thermal expansion coefficient. However, even this sputter-resistant material will eventually erode under the extended burn times of the ion engine typical for low thrust trajectories and deep-space missions [17,18]. In addition, long duration ion engine testing on the ground inevitably results in the deposition of back-sputtered carbon from the graphite panels of the facility walls onto the accelerator grid, causing significant uncertainties in performance and lifetime predictions [19,20].

Correcting for the facility effects to enable accurate assessment of the erosion rate for plasma facing materials in electric space propulsion devices, such as the accelerator grid of ion thrusters, ultimately requires prior knowledge of the sputtering characteristics of carbon. In spite of ongoing efforts over the past several decades, measuring the sputtering yield of carbon at low ion energies of 75–1000 eV relevant to electric space propulsion devices is non-trivial, because of the very low sputter yield of carbon [21–25]. Studies have reported large scatter in the measured sputter yield data particularly between measurements conducted in different laboratories, where the sputter yield can vary by nearly an order of magnitude at low ion energies [26,27]. The available sputter yield data for carbon also tends to be sparse at off-normal ion incidence angles, and extrapolation to the range of interest can introduce large errors. In addition, carbon has many different allotropes and exists in many polymorphs. The influence of different carbon structures on the sputtering yield characteristic is unknown. While many studies

* Corresponding author.
E-mail address: hbchew@illinois.edu (H.B. Chew).

https://doi.org/10.1016/j.carbon.2023.01.015
Received 3 November 2022; Received in revised form 5 January 2023; Accepted 8 January 2023
Available online 10 January 2023

have alluded to the similar sputtering yield and differential yield profiles between diamond, amorphous carbon, pyrolytic and isotropic graphite, as well as carbon-carbon composites [26,28,29], the underlying mechanism is unclear, given the significantly different physical and mechanical properties of these carbon structures. Studies also suggest that the measured sputtering yield may be sensitive to surface roughness, as evidenced by surface texturing on carbon films with height variations of ~0.2–0.3 μm [29,30]. For example, Deltschew et al. [27] reported a two-fold higher sputtering yield of exposed carbon fibers compared to graphite films, which they attribute to the unique and evolving surface morphology of these fibers. Material surface roughness can also significantly change the local incidence angle, and influence the trajectory of the sputterants, but the effect is challenging to quantify experimentally [29,31,32].

A well-developed analytical formula by Sigmund [33] has been widely adopted to estimate the sputter yield. Bohdansky [34] and Yamamura & Shindo [35] have since extended this formulation to cover a broader range of ion energies, and to account for very heavy or light ion sputtering as well as grazing ion incidence angles. Eckstein & Preuss [36] further augmented these formulas with an empirical-based correction factor specific for low energy sputter data. The semi-empirical or free parameters in these analytical formulas are typically calibrated against available data from experiments or simulation codes. On one hand, the experimental sputter yield data for carbon is very sparse and exhibits significant uncertainties in the low energy regime of interest (< 1 keV) to ion thrusters for electric space propulsion. On the other hand, Monte Carlo simulation codes, such as Transport of Ions in Matter (TRIM) or the Stopping Range of Ions in Matter (SRIM), are based on binary collision approximation, which breaks down at these low ion energies [37–40].

In this paper, we perform molecular dynamics (MD) simulations on the xenon ion bombardment of carbon substrates across an extensive range of ion energies and ion incidence angles, to resolve the uncertainties in the experimental sputter measurements. We describe the MD modeling in Section 2, and elucidate the atomistic mechanisms of sputter erosion, in relation to the initial carbon structure and sputtering conditions. In Section 3, we upscale our sputter yield predictions from MD to account for surface morphology effects, and adopt a Bayesian approach to calibrate the parameters of a semi-empirical sputter yield formula based on our results. Section 4 discusses the implications of our simulation results in the context of sputtering experiments in the literature. We conclude in Section 5 with a summary.

2. Molecular dynamics modeling

2.1. Approach

We perform MD simulations on the xenon ion bombardment of carbon substrates using LAMMPS [41]. The C–C interatomic interactions are governed by an Adaptive Intermolecular Reactive Empirical Bond Order (AIREBO) potential [42]. This potential allows for bond breaking and reforming, and accurately describes the sp-sp^2-sp^3 bond hybridization in carbon structures [43], along with the van der Waals long-range interactions typical for multilayer graphene (MLG) structures [44]. Separately, the Xe–Xe and Xe–C interactions are governed by a Ziegler-Biersack-Littmark (ZBL) potential [45], to account for screened nuclear repulsion associated with the high-energy collision between Xe–Xe or Xe–C atoms. As shown by our density functional theory (DFT) calculations (Fig. S1 of the Supplementary Materials), this ZBL potential accurately captures the interactions between xenon atom and various configurations of carbon atoms.

Majority of our ion bombardment simulations are performed on horizontally-oriented MLG (h-MLG), with the ABA stacking arrangement oriented normal to the vertical (z) axis (Fig. 1a). Our simulation box is periodic in the in-plane (x-y) directions with dimensions of 5.1 × 4.9 nm^2. We fix the bottom graphene layer throughout our simulations and designate the next two layers above as the damping layer to absorb the stress waves caused by ion impact. This follows with four heat bath layers above, which we introduce to equilibrate the system to the targeted temperature. Depending on the xenon ion incidence energy (E) and incidence angle (θ), we include multiple graphene layers above (9 layers in case of E = 500 eV in Fig. 1a) to ensure that the damage caused by the incident xenon ions is confined within the active graphene layers above the heat bath. In addition to h-MLG, we also perform ion bombardment simulations on diamond and vertically-oriented MLG (v-MLG). For the former, we assign one, two and four unit cells of diamond (lattice parameter of 3.567 Å) as the fixed, damping, and heat bath layers, with an active diamond substrate comprising of 14 × 15 × 8 unit cells above. Our ion bombardment simulations of v-MLG comprise of 15 graphene layers each of (y-z) dimensions 4.9 × 5.4 nm^2. Atoms from within the bottom 7 Å and the next 14 Å of these graphene layers are designated as the damping and heat bath zones, respectively. In addition, we attach a <001 > face-centered-cubic (FCC) Cu lattice structure to the bottom of these graphene layers, to provide structural rigidity and to capture the penetrated Xe ions channeling between these vertical

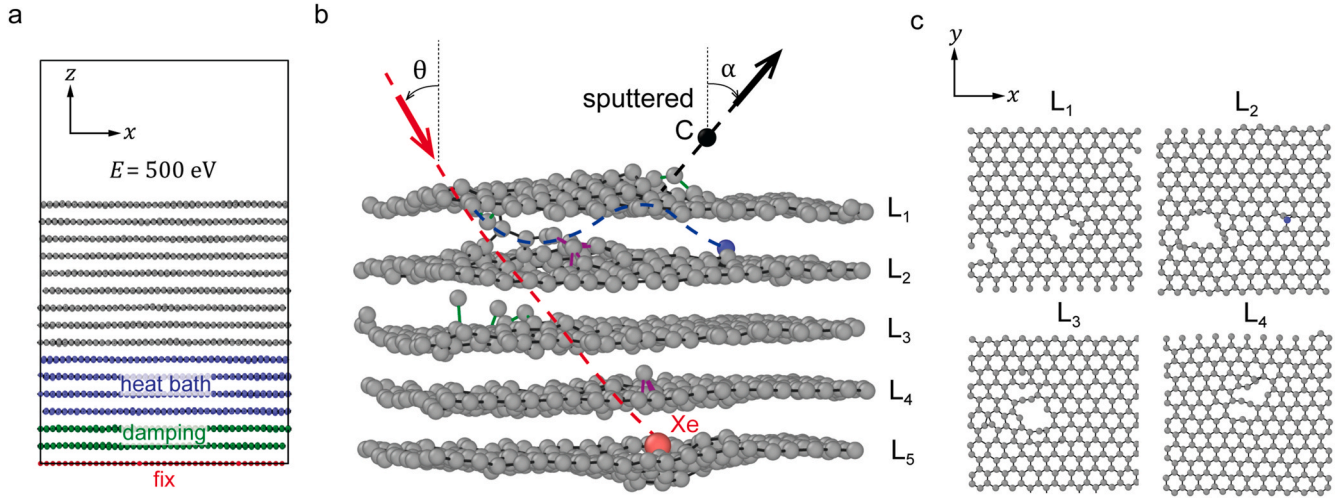

Fig. 1. (**a**) Horizontally-oriented multilayer graphene (h-MLG) with designated fixed, damping, and heat bath layers colored in red, green, and blue, respectively. (**b**) Side view of the atomistic configuration of h-MLG after the first xenon ion impact at an energy of E = 500 eV and incidence angle of θ = 30°. Green, black, and purple short lines denote sp, sp^2, and sp^3 bonds. Dashed red, blue, and black lines denote trajectory of the xenon ion, a knock-off carbon atom, and a sputtered carbon surface atom with sputtered angle, α. (**c**) Top-view of the atomistic configurations of the first four graphene layers corresponding to (**b**).

graphene layers. The interatomic interactions between Cu–Cu, Cu–C, and Xe–Cu atoms are governed by an Embedded Atom Method (EAM) potential [46], a Lennard-Jones (LJ) potential, and a ZBL potential, respectively, though the exact choice of these potentials will not affect the sputtering simulations since this Cu lattice is sufficiently far from the v-MLG surface.

Prior to initiating the bombardment sequence, we adopt a time step of 1 fs and subject the entire carbon structure sans the fixed layer to an NVT ensemble maintained at a temperature of 400 K by a Berendsen thermostat for 30 ps, which is a typical surface temperature from a beam dump experiment [18]. We then switch off the thermostat and perform the ion bombardment simulations using a time-accelerated scheme as follows. For each ion bombardment, we deposit one xenon atom randomly above the substrate surface with an initial ion velocity (v_x, v_y, v_z) constrained to have the designated ion (kinetic) energy, E, of between 75 and 2000 eV, and ion incidence angle, $\theta = \text{atan}(\sqrt{v_x^2 + v_y^2}\,/v_z)$, of between 0° and 75°. The exact choice of (v_x, v_y, v_z) is randomly selected at the start of the simulation but is fixed between the successive bombardments of a given set of (E, θ) to simulate a constant ion beam source. We allow the system to equilibrate without a thermostat for the first 1 ps, with a time step of 0.1 fs, to resolve the initial impact dynamics associated with the deposition process. Using a time step of 1 fs, we then switch on the thermostat in the heat-bath region and set it to the target temperature of 400 K for the next 20 ps, before quenching the entire system to 400 K for a further 20 ps. We then repeat this entire process for the next ion bombardment. By accelerating the time between each bombardment sequence, our simulation predictions (e.g. sputter yield) are now in terms of the ion fluence, defined as the number of bombarded xenon ions per unit in-plane (x-y) area.

2.2. Results

Our MD simulations show that the penetration of xenon ions within the graphite layers at high velocities causes significant disruption to the atomic arrangement of carbon atoms along its path. Fig. 1b shows the side view of the atomic configuration of the graphitic substrate after the first xenon ion impact with an ion energy of $E = 500$ eV and ion incidence angle of $\theta = 30°$. The heavier and significantly larger xenon atom knocks-off multiple carbon atoms, leading to a collision cascade along its path (red dashed line), before residing between the L_4 and L_5 graphene interlayers. The subsequent collision of one of these knock-off carbon atoms (colored in blue with trajectory in blue dashed line) leads to sputtering of a surface carbon atom (black) with sputtered angle α and a kinetic energy of ~20 eV. The bombardment process results in the breaking of sp^2 bonds (black) to form sp bonds (green), as well as a small percentage of sp^3 bonds (purple). In addition, multiple pores are created within the first four graphene interlayers (L_1 to L_4 in Fig. 1c) along both the xenon ion path and at the location of the sputtered carbon atom (L_1).

Repeating the bombardment process above increases the density of sp bonds at the expense of sp^2 bonds, and results in amorphization of the graphitic subsurface spanning the penetration depth of the xenon ion. We partition the evolving atomistic structure into vertical bins of 0.335 nm representing the interlayer spacing, and average the proportion of sp and sp^2 bonds within each bin. Fig. 2a–d shows the atomistic structure and the spatial distribution of sp versus sp^2 bond proportions corresponding to four fluences. At low ion fluence of 1×10^{14} ion/cm^2, chains of sp-bonded C–C atoms form across the damaged interlayers, but the layered h-MLG structure is still distinct (Fig. 2a). Increasing the fluence to 4×10^{14} ion/cm^2 leads to a more porous and homogeneous carbon structure, with increasing (decreasing) proportion of sp (sp^2) bonds towards the exposed surface (Fig. 2b). These trends continue until an almost equal proportion of sp and sp^2 bonds are formed at the surface

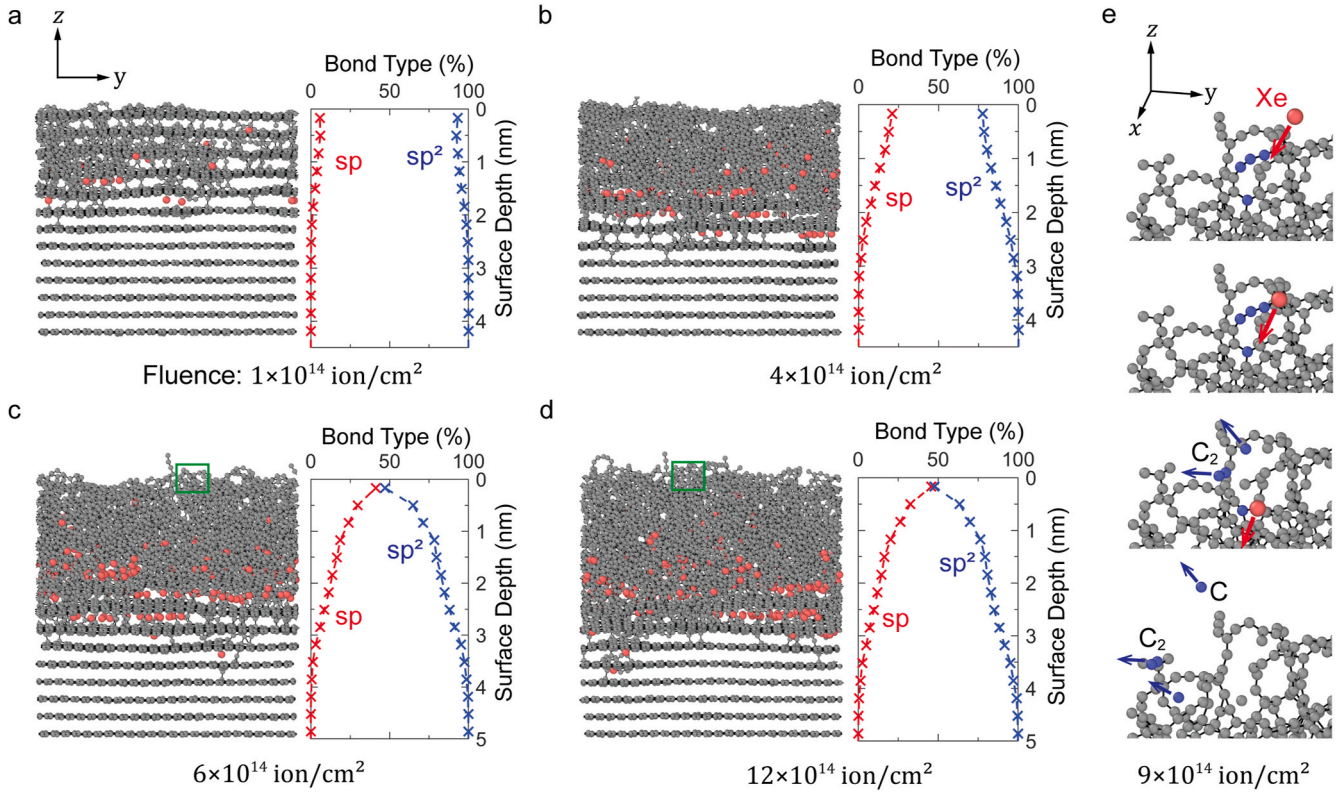

Fig. 2. (**a-d**) Atomistic configuration (left) and corresponding spatial distribution of sp and sp^2 bond proportions (right) of h-MLG subjected to ion energy of $E = 500$ eV and ion incidence angle of $\theta = 30°$ at four ion fluences. (**e**) Close-up view [green box in (**c,d**)] depicting the sputtering sequence initiating with scission of sp and sp^2 bonded C–C chains (blue atoms) along the xenon ion path (red atom), leading to the ejection of 2 single and 1 duo carbon atoms from the surface. Arrows denote trajectory of xenon (red) and sputtered carbon atoms (blue).

(Fig. 2c). Beyond this fluence, steady-state sputtering is achieved, and the spatial distribution of sp versus sp^2 bond proportions, indicative of the structural characteristics of the amorphous subsurface, remains unchanged under further ion bombardment (compare Fig. 2c and d). Fig. 2e shows snapshots of the typical steady-state sputtering sequence, caused by scission of both sp and sp^2 bonded C–C chains (blue atoms) along the xenon ion path (red atom, arrow), leading to the ejection of 2 single and 1 duo carbon atoms from the surface (Movie S1 of the Supplementary Materials). Similarly, we have traced the origin of the sputtered carbon species under steady-state bombardment across different E and have found that the sputtered species consistently originate from the exposed surface due to the higher proportion of weaker sp bonds (Fig. S2 of the Supplementary Materials). Unlike metallic materials, the carbon substrate traps xenon ions within the subsurface to a much higher degree, with the xenon absorption rate ranging from ~10% at $E = 200$ eV, $\theta = 60°$ to ~100% at $E = 1$ keV, $\theta = 0°$ (Fig. S3 of the Supplementary Materials). This high xenon absorption rate will significantly bias mass loss measurements for quantifying the sputtering yield in experiments [29,47,48].

Supplementary video related to this article can be found at https://doi.org/10.1016/j.carbon.2023.01.015

We average the percentage of sp and sp^2 bonds, as well as the atomic density, within the volume of the amorphized region bounded by the average xenon ion penetration depth (Fig. S3 of the Supplementary Materials) and α-shapes surface reconstruction [49] at each fluence, to quantify the evolving bond fraction and porosity in the amorphous subsurface. Figs. 3 and 4 show these evolving structural characteristics with ion fluence for three representative ion energies of $E =$ 200, 500 and 1000 eV, and at four ion incidence angles of $\theta = 0°$, 30°, 45° and 60°. In all cases, the decrease in the sp^2 bond percentage with ion fluence is accompanied by a corresponding increase in the sp bond percentage (Fig. 3) – the percentage of both these bond types under steady-state bombardment (arrows) sum to 96%, with the remaining 4% attributed to sp^3 bonds. In addition to these changes in the bond types, the structure also becomes increasingly porous with bombardment, as shown by the decrease in atomic density ρ (Fig. 4). Beyond a certain fluence (arrows in Figs. 3 and 4), both the sp/sp^2 bond fractions and ρ reach a plateau, with nearly identical steady-state values for different E and θ. This suggests that the amorphous subsurface structures created by different ion energies and ion incidence angles are virtually indistinguishable from one another under steady-state bombardment. We have repeated these calculations across a wider range of E and θ, and have summarized the near-uniform steady-state sp/sp^2 bond fractions and ρ in Fig. S4 of the Supplementary Materials.

Our amorphous subsurface structures above are created by the xenon ion bombardment of h-MLG. We repeat our ion bombardment simulations on sp^3-bonded crystalline diamond with $E =$ 1 keV, $\theta =$ 45° (Fig. 5a), as well as v-MLG with $E = 700$ eV, $\theta = 30°$ (Fig. 5b). The initial evolution of the sp/sp^2 bond proportion (Fig. 5c) and the atomic density ρ (Fig. 5d) is sensitive to the initial crystal structure. For v-MLG (blue curves), the increase in sp bond proportion with fluence is accompanied by a decrease in sp^2 bond proportion, which is similar to h-MLG. In contrast, for the diamond substrate (red curves), both proportions of sp and sp^2 bonds are converted from sp^3 bonds during the bombardment process, and monotonically increase with fluence. In addition, because of the more-densely packed nature of sp^3-bonded diamond, the drop in ρ (increase in porosity) for the diamond substrate with fluence is also more pronounced compared to v-MLG. Nevertheless, under steady-state bombardment, both the proportion of sp/sp^2 bonds and the atomic densities plateau to the exact same values as for h-MLG (average steady-state values across all h-MLG cases simulated denoted by dashed black lines). Thus, the "steady-state" amorphous carbon subsurface structures created by ion bombardment appear to be independent of *both* the sputtering conditions (E, θ), as well as the initial carbon structure. We track the accumulated quantity of sputtered carbon as a function of ion fluence for both diamond (red solid line) and v-MLG (blue solid line) in

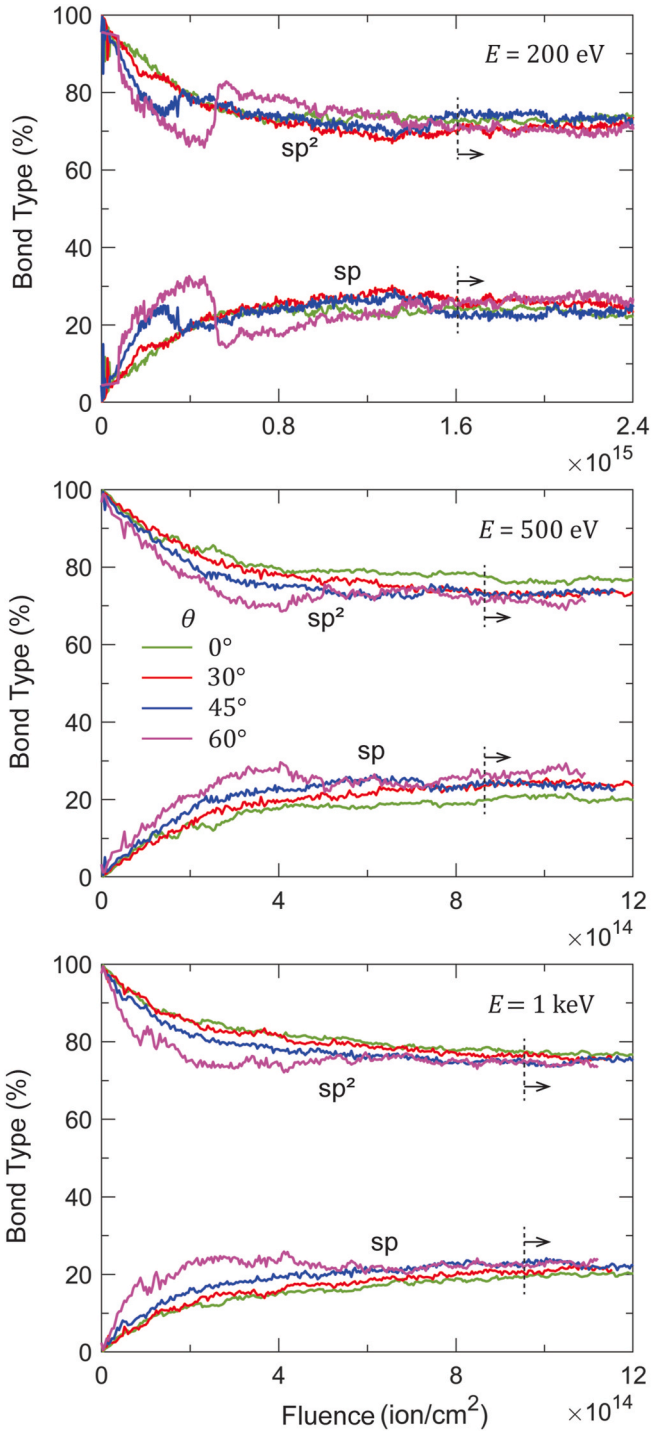

Fig. 3. Evolution of the average percentage of sp and sp^2 bonds within the amorphized subsurface with ion fluence for ion energies of $E =$ 200, 500, and 1000 eV, and at ion incidence angles of $\theta = 0°$, 30°, 45° and 60°. Arrows denote steady-state sputtering regime.

Fig. 5e and include the results for h-MLG under the same sputtering conditions as for diamond (red dashed line) and v-MLG (blue dashed line). While the diamond structure has the highest initial sputtering yield, as defined by the slope of the curves in Fig. 5e, the sputtering yields under steady-state conditions (arrows) are nearly identical for diamond and h-MLG, as well as v-MLG and h-MLG, under the same E and θ. This confirms that the bombardment process creates a unique amorphous subsurface structure that is independent of both the initial carbon structure (e.g., diamond, v-MLG, and h-MLG), and the sputtering history

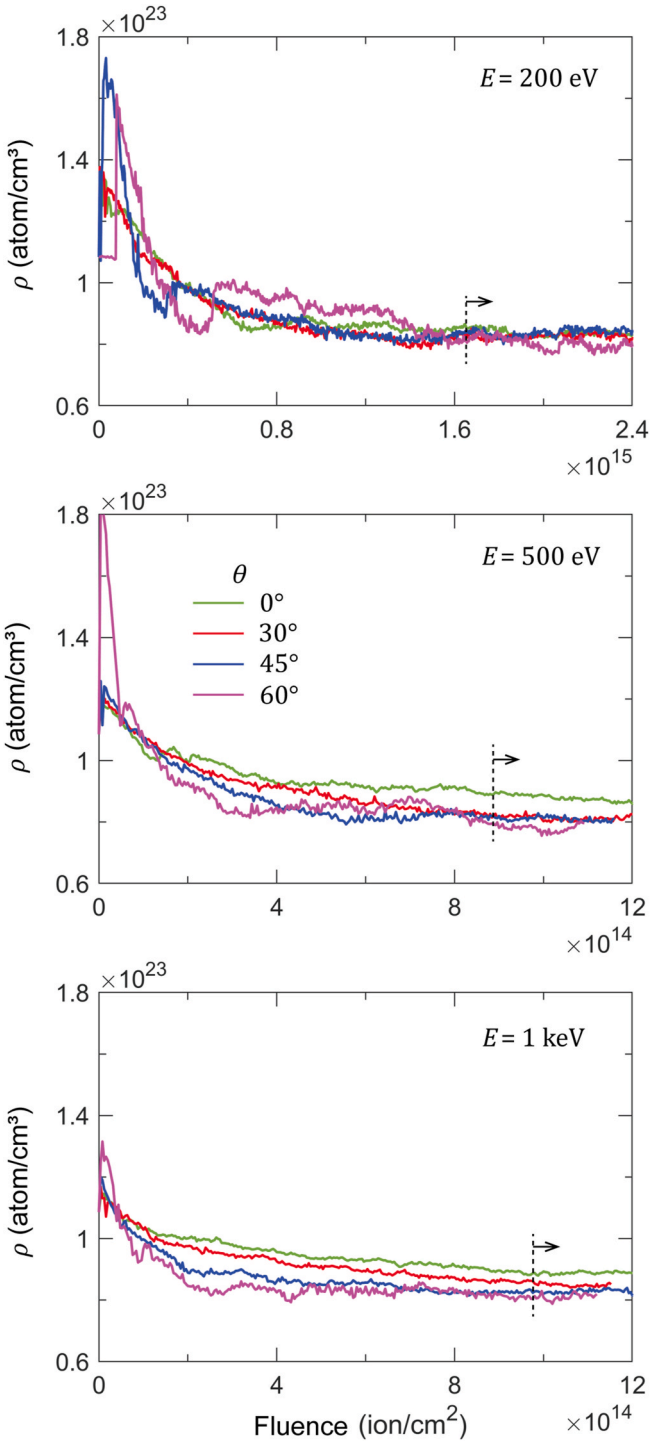

Fig. 4. Evolution of the atomic density, ρ, within the amorphized subsurface with ion fluence for ion energies of $E = 200$, 500, and 1000 eV, and at ion incidence angles of $\theta = 0°$, 30°, 45° and 60°. Arrows denote steady-state sputtering regime.

(prior E and θ). Consequently, the measured steady-state sputtering yield from all these different initial carbon structures will be identical.

We summarize the steady-state sputtering yield from MD simulations across different E and θ in Fig. 6 (blue symbols). Note that these MD results are based on the xenon ion bombardment of an initial h-MLG structure, with exception for $E = 75$ eV (all θ) where we adopt the steady-state amorphous structure created from h-MLG subjected to $E = 200$ eV ($\theta = 45°$) as the starting initial configuration for our ion bombardment simulations to reduce computational time. In fact, starting with h-MLG at $E = 75$ eV may not result in carbon sputtering because of the strong in-plane sp^2 bonds. We include the sputtering yield from existing experimental studies in the literature (black symbols), as well as our calculations from SRIM models (purple symbols) [39]. As prior studies have shown, SRIM calculations based on binary collision approximation tend to be inaccurate at ion energies of below ~1 keV, due to the inability to handle many-body collisions of arbitrarily many atoms [40,50]. Similarly, our sputtering yield predictions from SRIM tend to deviate from MD predictions at $E <\sim 1$ keV. More importantly, our MD results on the sputtering yield are generally in good agreement with experimental measurements at intermediate θ across the ion energy range of 75 eV $\leq E \leq$ 2 keV, but under and overpredicts the sputtering yield at $\theta = 0°$ and 60°, respectively. We attribute this to surface morphology effects, detailed later in Section 3, which are beyond the length-scales of MD simulations.

In addition to the sputtering yield, the differential sputter yield profile, representing the probability density function (PDF) $f(\alpha)$ of the angle of the carbon sputterants, α, is equally essential to quantifying the contributions of redeposition (contamination) effects on plasma facing materials, including those of solar cells, fusion reactors, and electric propulsion facilities [20,51–55]. From MD simulations, we trace the local angle of emission α of the carbon sputterants (Fig. 1b) ranging from −90° to 90° with respect to the surface normal under steady-state bombardment, to construct $f(\alpha)$ for sputterant emission in Fig. 7, at ion energies of $E = 200$, 500, 1000 and 2000 eV and at four ion incidence angles of $\theta = 0°$, 30°, 45° and 60°. Each symbol in Fig. 7 represents a cumulative probability density based on the sum of all sputterants across the azimuthal angles over a bin size of ±10° from the indicated α value. Our results show that the profile of $f(\alpha)$, while primarily a function of θ, is independent of E. The PDF profile transitions from near-uniform distribution of sputterants across a wide range of α for $\theta = 0°$, to having a skewed distribution at higher θ favoring the forward scatter direction with maximum distribution of sputterants centered at $\alpha \simeq 50°$. In addition, $f(\alpha)$ at a specific θ can be well described by a linear combination of two Gaussian function distributions (blue curve in Fig. 7), each representing the dominant forward ($0° < \alpha < 90°$) and backward ($-90° < \alpha < 0°$) scatter directions

$$f(\alpha) = \frac{A}{\sigma_1\sqrt{2\pi}} e^{-\frac{1}{2}\left(\frac{\alpha-\mu_1}{\sigma_1}\right)^2} + \frac{1-A}{\sigma_2\sqrt{2\pi}} e^{-\frac{1}{2}\left(\frac{\alpha-\mu_2}{\sigma_2}\right)^2} \quad (1)$$

where μ_j represents the peak sputtered angle, σ_j the spread due to the inelastic collisions, and A the relative contribution of the forward ($j = 1$) and backward ($j = 2$) sputterants. The fitting parameters for μ_j, σ_j, A are summarized in Table S1 of the Supplementary Materials.

3. Surface morphology modeling

Scanning electron microscopy (SEM) imaging of amorphous carbon films show the surface, while macroscopically smooth, appears very rough at lower (micrometer) length-scales (Fig. 8a) [47]. Atomic force microscopy (AFM) measurements of the surface height map (Fig. 8b) show the surfaces to have height variations (amplitude) on the order of $\frac{H}{2} \simeq 200$ nm [47]. In addition, there are a total of 12 peaks within the 5 × 5 μm^2 surface height map, which infers a wavelength of $\lambda \simeq 2$ μm. For simplicity, we represent the surface morphology in one-dimension by a cosine function

$$h = \frac{H}{2}\cos\left(\frac{2\pi x}{\lambda}\right) + \frac{H}{2} \quad (2)$$

As depicted schematically in Fig. 8c, the surface normal $\boldsymbol{n}$ now varies with location x along the surface. Hence, the local incident angle, θ_L, at the surface impact point is now distinct from the global ion incidence angle θ. Note that the sputtering yield predictions from MD (Fig. 6) are

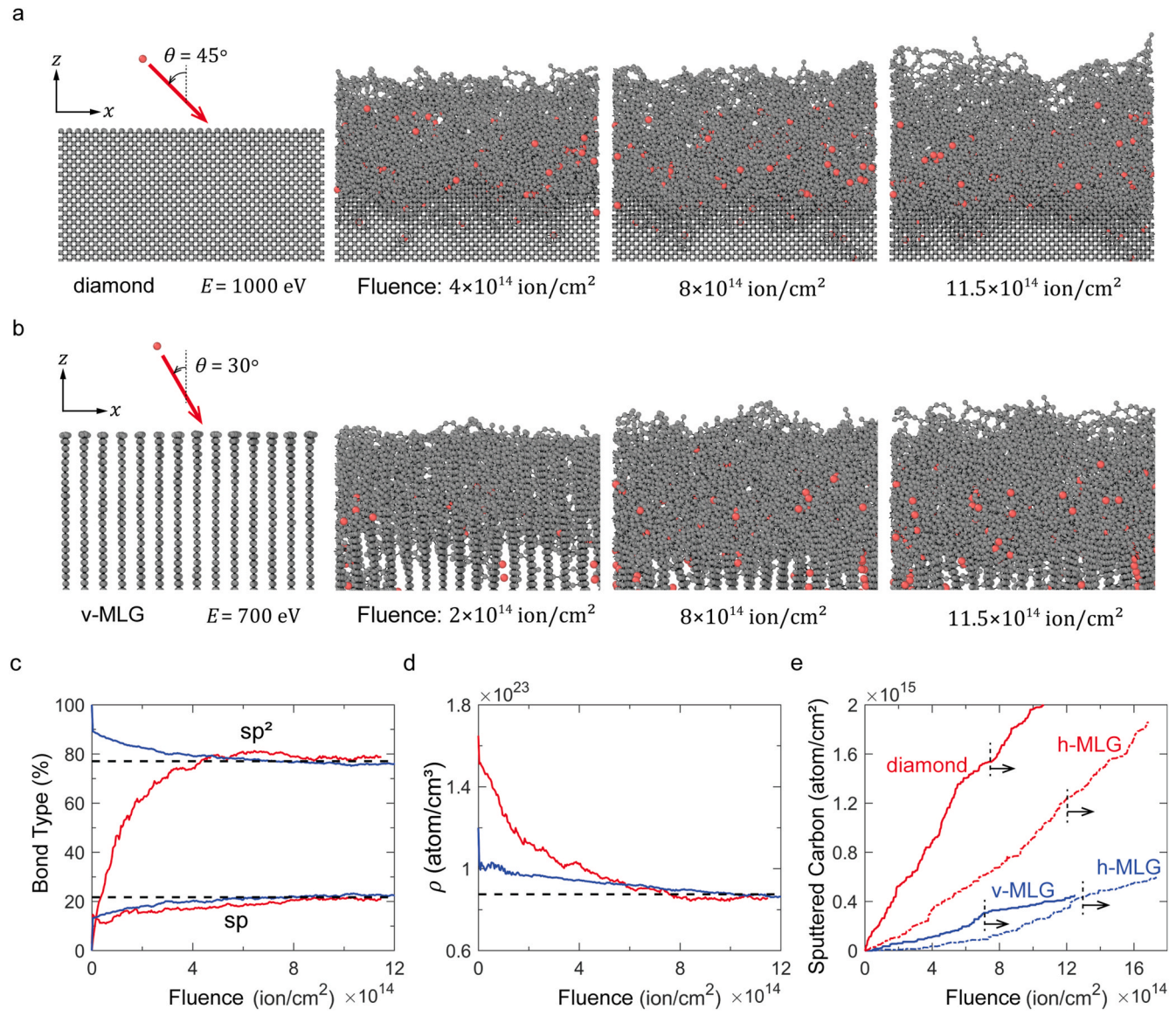

Fig. 5. (**a**,**b**) Evolution of the atomistic configurations with ion fluence for diamond with $E = 1$ keV, $\theta = 45°$ (**a**), and for vertically-oriented multilayer graphene (v-MLG) with $E = 700$ eV, $\theta = 30°$ (**b**). (**c**,**d**) Evolution of the proportion of sp and sp^2 bonds (**c**) and atomic density ρ (**d**) within the amorphous subsurface for diamond (red) and v-MLG (blue). Dashed black lines denote average values for h-MLG under steady-state bombardment. (**e**) Total quantity of sputtered carbon atoms with fluence for diamond (solid red line) and v-MLG (solid blue line), as compared to h-MLG under the same E, θ (corresponding dashed red, and blue lines). Arrows denote the steady-state sputtering regime.

with respect to the surface normal $\boldsymbol{n}$, and hence are based on local ion incidence angle θ_L. The continuous variation of θ_L along the surface in turn causes the sputtering yield $Y_{\mathrm{MD}}(E, \theta_L)$ to vary even for ion bombardment with uniform θ. Because of the undulating surface, however, only a proportion K of the sputterants can escape from the surface (purple arrows in Fig. 8c), while the remaining proportion $D\ (= 1 - K)$ is redeposited back onto the surface (green arrows in Fig. 8c). The values of K and D are the cumulative probability of $f(\alpha)$ (Fig. 7) over the domains that can be delineated by lines joining the ion impact site, and the surface peaks within the field-of-view (dashed purple line in Fig. 8c). In addition, the undulating surface shields a portion of the surface, between the limits of $x_s < x < x_e$ in Fig. 8d, from the incoming ions.

Accounting for all three surface morphology effects, the effective sputtering yield can be expressed as

$$Y\left(\frac{H}{\lambda}, E, \theta\right) = \frac{\int_0^{\lambda} KY_{\mathrm{MD}}[1 - \mathrm{stp}(x - x_s) + \mathrm{stp}(x - x_e)]\xi dx}{\int_0^{\lambda} \xi dx} \tag{3}$$

where $\mathrm{stp}(x)$ denotes a unit step function, and $\xi(\theta,x)$ is the local ion fluence representing the variation of ions impacting the undulating surface per unit elemental dimension dx. Note that ξ is constant when $\theta = 0°$. We remark that this simple model does not account for surface curvature effects, which are only apparent at high ion energies ($>\sim 5$ keV) and at very small λ ($<\sim 100$ nm) where the impact-induced damage can span across multiple nanoripples [30,56,57]. For a perfectly smooth surface, i.e. $\frac{H}{\lambda} = 0$, we obtain $Y = Y_{\mathrm{MD}}$. For $\frac{H}{\lambda} > 0$, we assume a constant incoming ion fluence at the far-field, and solve (3) numerically by discretizing the domain $0 \le x \le \lambda$ into individual elements, each with a constant K and Y_{MD}. We consider the cumulative contributions of local incidence angle, surface redeposition, and surface shielding effects on the effective steady-state sputtering yield Y as a function of $\frac{H}{\lambda}$ in Fig. 9. Results show that the changes in the local incidence angle (dashed dot line) significantly changes the sputtering yield across all θ, and represents the most significant effect of surface morphology. This inclusion of surface redeposition effect (thick dashed

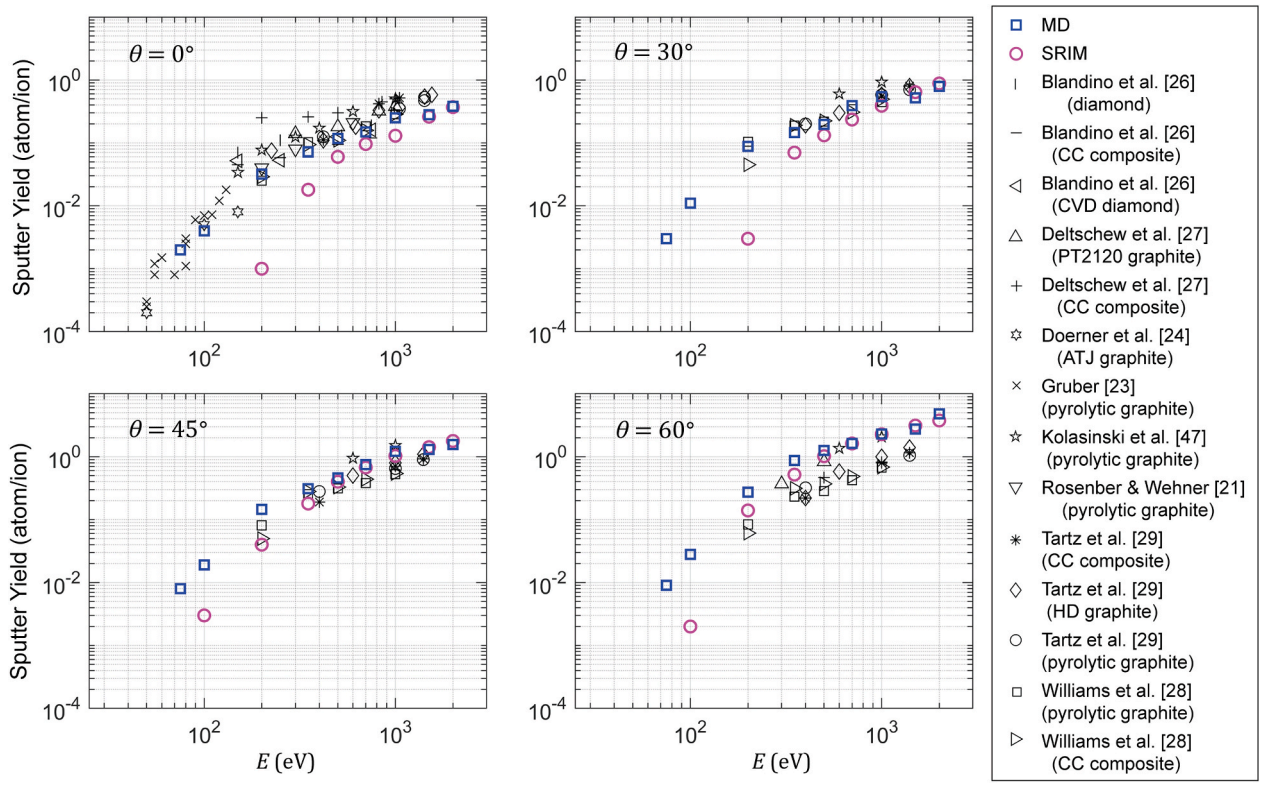

Fig. 6. Steady-state sputtering yield from MD simulations (blue symbols) and SRIM calculations (purple symbols) versus experiments for different carbon structures (black symbols) across various E and θ.

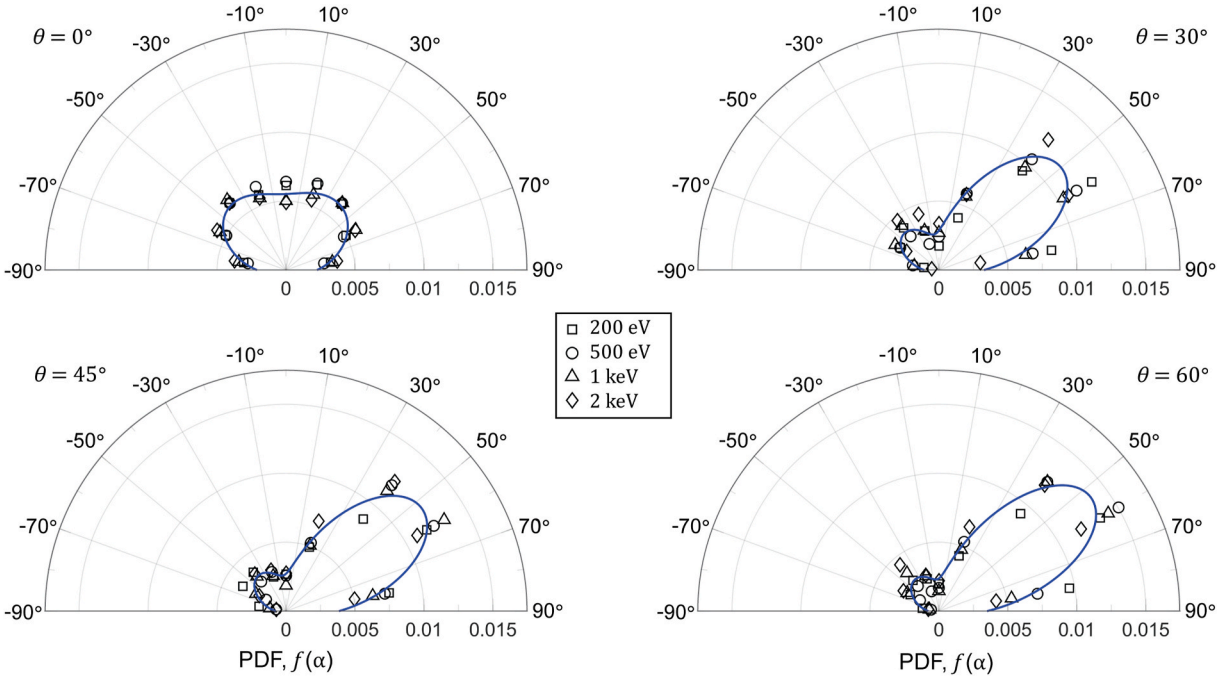

Fig. 7. Probability density function (PDF) of the differential yield profile of the sputterants, $f(\alpha)$, from MD simulations, at $E = 200$, 500, 1000 and 2000 eV with $\theta = 0°$, 30°, 45° and 60°. Each symbol denotes the cumulative probability density over all azimuthal angles within a bin size of $\Delta\alpha = \pm 10°$. Blue curve shows the average fitting over all E for each θ, based on a linear combination of two Gaussian distribution functions.

line), however, lowers the sputtering yield and partially mitigates the influence of local incidence angle changes for $\theta \leq 45°$. In contrast, surface shielding effect is only visible at high $\frac{H}{\lambda}$ coupled with high θ of 60°. When all three contributions are considered (solid line), our results show that the effects of $\frac{H}{\lambda}$ are especially dominant at higher ion incidence angles of $\theta = 60°$, where we observe a several-fold drop in the sputtering yield for $E = 500$ eV, at $\frac{H}{\lambda} \simeq 0.2$ representative of amorphous carbon films (Fig. 8a and b). We summarize our steady-state sputtering yield

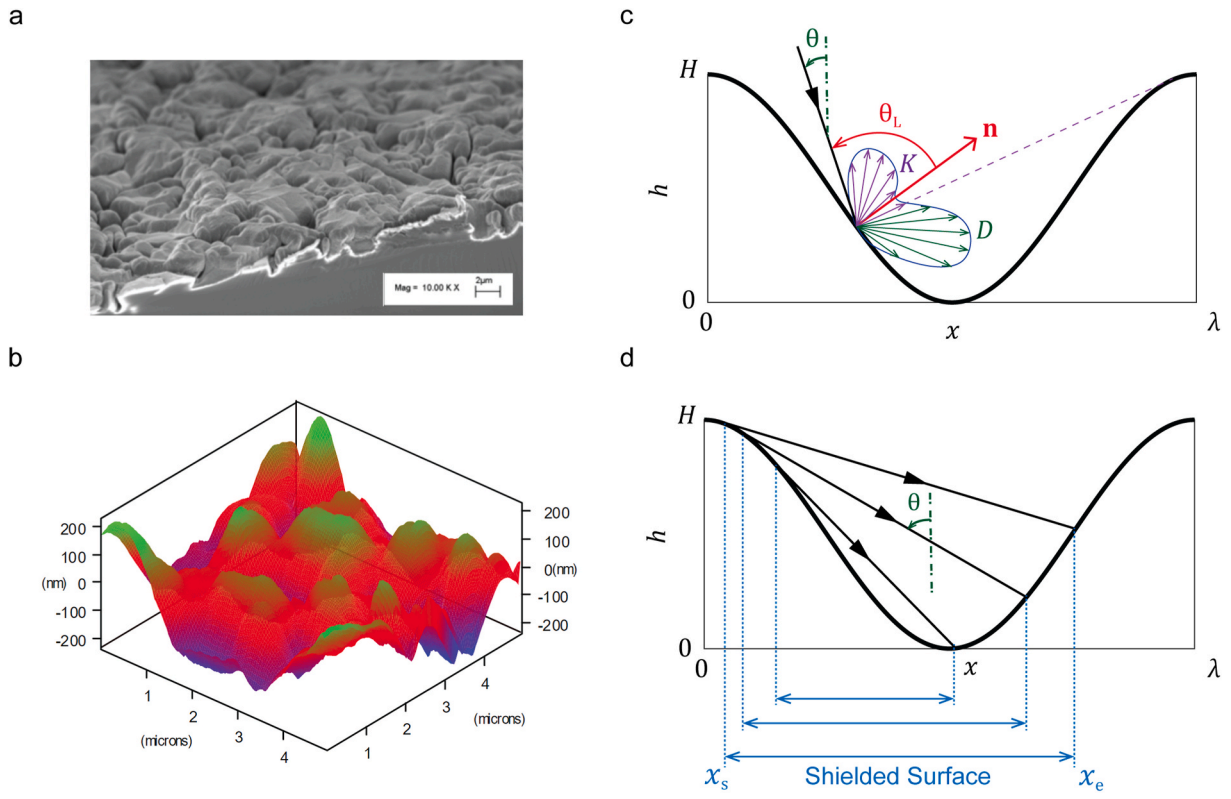

Fig. 8. (**a,b**) Scanning electron microscopy (SEM) imaging (**a**) and atomic force microscopy (AFM) surface height measurements (**b**) of amorphous carbon films [47]. (**c,d**) Schematic of an idealized surface geometry represented by a cosine function with amplitude $H/2$ and wavelength λ, depicting changes in the local incidence angle θ_L from the global ion incidence angle θ at the impact site, redeposition of the sputterants D to only allow the proportion K to escape (**c**), along with the shielding of a portion of the surface, $x_s < x < x_e$, from the incoming ions (**d**).

predictions, corrected for surface morphology effects ($\frac{H}{\lambda} = 0.2$) in Fig. 10 (blue symbols). Our augmented MD predictions are now well within the experimental scatter across the range of ion energies and ion incidence angles.

Empirical and semi-empirical models to describe the sputtering yield commonly assume that the energy and angular dependence are separable, i.e.

$$Y(E,\theta) = Y(E,0)Y^{'}(\theta) \tag{4}$$

here, we will adopt the formalism by Eckstein & Preuss [36], where the energy dependence of the sputtering yield at normal incidence can be expressed as

$$Y(E,0) = Qs_n \frac{\left(\frac{E}{E_{th}} - 1\right)^{\mu}}{\frac{\lambda}{w} + \left(\frac{E}{E_{th}} - 1\right)^{\mu}} \tag{5}$$

$$w = \varepsilon + 0.1728\sqrt{\varepsilon} + 0.008\varepsilon^{0.1504}$$

with the multiplicative factor for angular dependence

$$Y^{'}(\theta) = (\cos(\theta^c))^{-f} \exp\left(b\left(1 - (\cos(\theta^c))^{-1}\right)\right) \tag{6}$$

where s_n in (5) is the nuclear stopping cross section in the form of a Krypton–Carbon potential relevant to the low energy bombardment of xenon ions on carbon species [50,58], and is expressed as

$$s_n = \frac{0.5\ln(1 + 1.2288\varepsilon)}{1 + 0.1728\sqrt{\varepsilon} + 0.008\varepsilon^{0.1504}} \tag{7}$$

with the reduced nuclear stopping power

$$\varepsilon = \frac{a_L}{Z_i Z_S} \frac{4\pi\varepsilon_0}{e^2} \frac{M_s}{M_i + M_s} E \tag{8}$$

where $\varepsilon_0 = 1.42 \times 10^{-40}\ \mathrm{C^2 eV^{-1} \mathring{A}^{-1}}$ is the vacuum permittivity, $e = 1.602 \times 10^{-19}$ C is the elementary charge, (M_i, Z_i) and (M_S, Z_S) are the (atomic mass, atomic number) for xenon and carbon atoms and are taken to be $(131.293\ \mathrm{g\ mol^{-1}}, 54\ \mathrm{amu})$ and $(12.011\ \mathrm{g\ mol^{-1}},\ 6\ \mathrm{amu})$, respectively, and a_L is the Lindhard screening length

$$a_L = \left(\frac{9\pi^2}{128}\right)^{\frac{1}{3}} a_0 \left(Z_i^{\frac{2}{3}} + Z_s^{\frac{2}{3}}\right)^{-\frac{1}{2}} \tag{9}$$

with the Bohr radius, $a_o = 0.529$ Å.

The parameters $(Q, \lambda, \mu, E_{th})$ in (5) along with (b, c, f) in (6) can be regarded as physics-based fitting parameters for the energy and angular dependence portions of the semi-empirical sputtering model. Notably, Q is the scaling representing the spread of the impact energy between the ion and the target, λ, μ describes the strength and the onset of the sputtered yield at low ion energy, E_{th} denotes the threshold energy for sputtering, f scales with the proportion of the particle reflection coefficient, while b, c controls the peak sputter yield angle [36]. We employ Bayesian parameter estimation, applied to the MD dataset of the sputtering yield augmented to account for surface morphology effects ($\frac{H}{\lambda}$), to generate posterior probability distributions for these semi-empirical parameters. Because the sputtering yield at our lowest simulated ion energy of $E = 75$ eV is several orders of magnitude smaller than the sputtering yield at $E = 2$ keV (Fig. 10), parameter estimation in the linear space would incorrectly negate the lower energy dataset in favor of the higher energy dataset because of their significantly higher sputtering rates. Instead, we transform (4)–(6) to the natural logarithmic space to allow the MD dataset across the entire ion energy range of

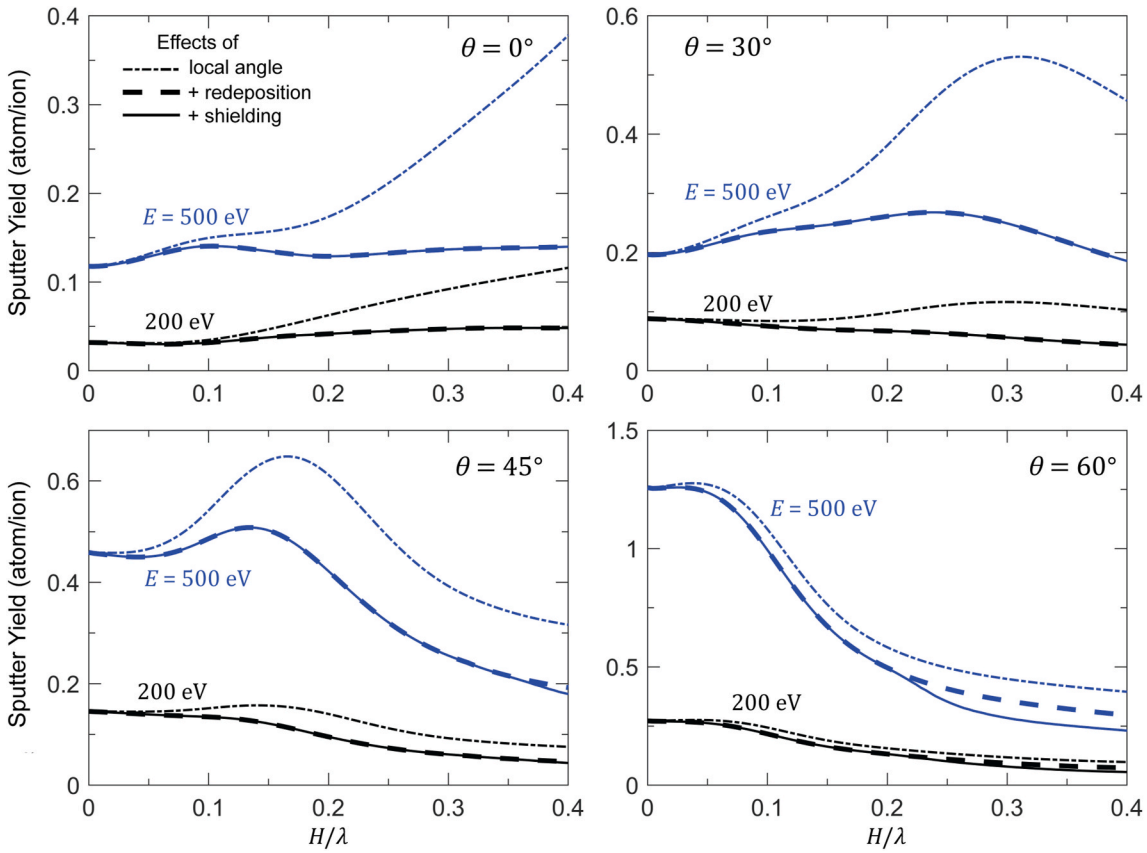

Fig. 9. Changes in the effective steady-state sputter yield Y with $\frac{H}{\lambda}$ for $E = 200$ and 500 eV at $= 0°$, 30°, 45° and 60°, considering the cumulative contributions of local incidence angle, surface redeposition, and surface shielding effects.

75 eV $\leq E \leq$ 2 keV to be adequately considered in a Markov chain Monte Carlo algorithm (MCMC) with Delay Rejection Adaptive Method (DRAM) [59]. We summarize in Table 1 the fitting parameters of the Eckstein & Preuss [36] sputter model that yield the maximum likelihood curve based on MD results for varying $\frac{H}{\lambda}$. For completeness, we also include parameters fitted to the experimental sputter yield data of the various polymorphs of carbon (black symbols in Fig. 10) at normal ion incidence angle [60]. We observe significant changes to these maximum likelihood parameters with $\frac{H}{\lambda}$, which demonstrates the sensitivity of the sputtering data to surface morphology. Based on the maximum likelihood parameters for $\frac{H}{\lambda} = 0.2$ (see PDF of the fitting parameters in Fig. S5 of the Supplementary Materials), we include in Fig. 10 the sputtering yield from the newly-calibrated Eckstein & Preuss [36] model (blue curves), along with the likelihood bounds of $\pm 3\sigma$ (shaded grey), where σ is the standard deviation. The fitted results are in near perfect agreement with MD data across all E and θ, with the likelihood bounds encompassing most of the experimental data.

In addition to changes in the sputter yield predictions, the effects of surface morphology can induce changes to the apparent differential yield profile with respect to the global (x,y,z) coordinate system. Here, we quantify the local sputter yield profile over all discretized surface elements between 0 and λ, to obtain the effective PDF of the differential yield profile $f(\alpha)$ for different $\frac{H}{\lambda}$ in Fig. 11. We summarize the parameters of (1) for different $\frac{H}{\lambda}$ in Table S1 of the Supplementary Materials. Our results generally show that surface morphology has minimal effects on $f(\alpha)$, except at very high $\frac{H}{\lambda}$ of 0.3 with ion incidence angles of $\theta \geq 30°$, where a higher proportion of sputterants with $|\alpha| < 20°$ is favored since redeposition effects at higher $|\alpha|$ are exacerbated due to the steeper surface.

As aforementioned, differential yield profile measurements for carbon sputtering within the low ion energy regime ($\leq$ 1 keV) of interest are extremely limited. Using a Quartz Crystal Microbalance (QCM), Williams et al. [28] reported the differential yield profile as a function of polar angle α by measuring the quantity of detected carbon sputterants per incident xenon ion per unit steradian. However, the measured data for each polar angle α was only collected at a fixed azimuthal angle, and a uniform sputterant distribution was assumed along the azimuthal direction. We include in Fig. 11 the equivalent $f(\alpha)$ from data provided by Williams et al. [28] at various E (black symbols). The experimental data for $E \geq 500$ eV are in reasonable agreement with our MD-predicted $f(\alpha)$ spanning the range of possible surface morphologies ($0 \leq \frac{H}{\lambda} \leq 0.3$). The experimental data, however, deviates from our simulation results in the backward scatter directions (i.e., $\alpha < 0°$) for $E \leq 350$ eV, and is in contrast to our MD results which show $f(\alpha)$ to be independent of E (Fig. 7). Presumably, this discrepancy arises from the assumption of uniform distribution of sputterants along the azimuthal angle in the experimental measurements, which artificially enforces $f(\alpha) \to 0$ when $\alpha \to 0°$. In comparison, we account for all detected carbon sputterants along the azimuthal angles for each polar angle data in our construction of $f(\alpha)$ from MD simulations (Fig. 7).

4. Discussions

A starting point of predicting the sputtering yields for any ion-target combination is through semi-empirical analytical formulas, including those by Sigmund [33], Yamamura & Shindo [35], and Eckstein & Preuss [36]. The free parameters of these formulas are commonly fitted to models based on binary collision approximation, such as SRIM or TRIM [38,39]. However, the differences between the sputtering yield data on carbon from experiments (black symbols in Fig. 6) and those from SRIM or TRIM models (purple symbols in Fig. 6) can differ by

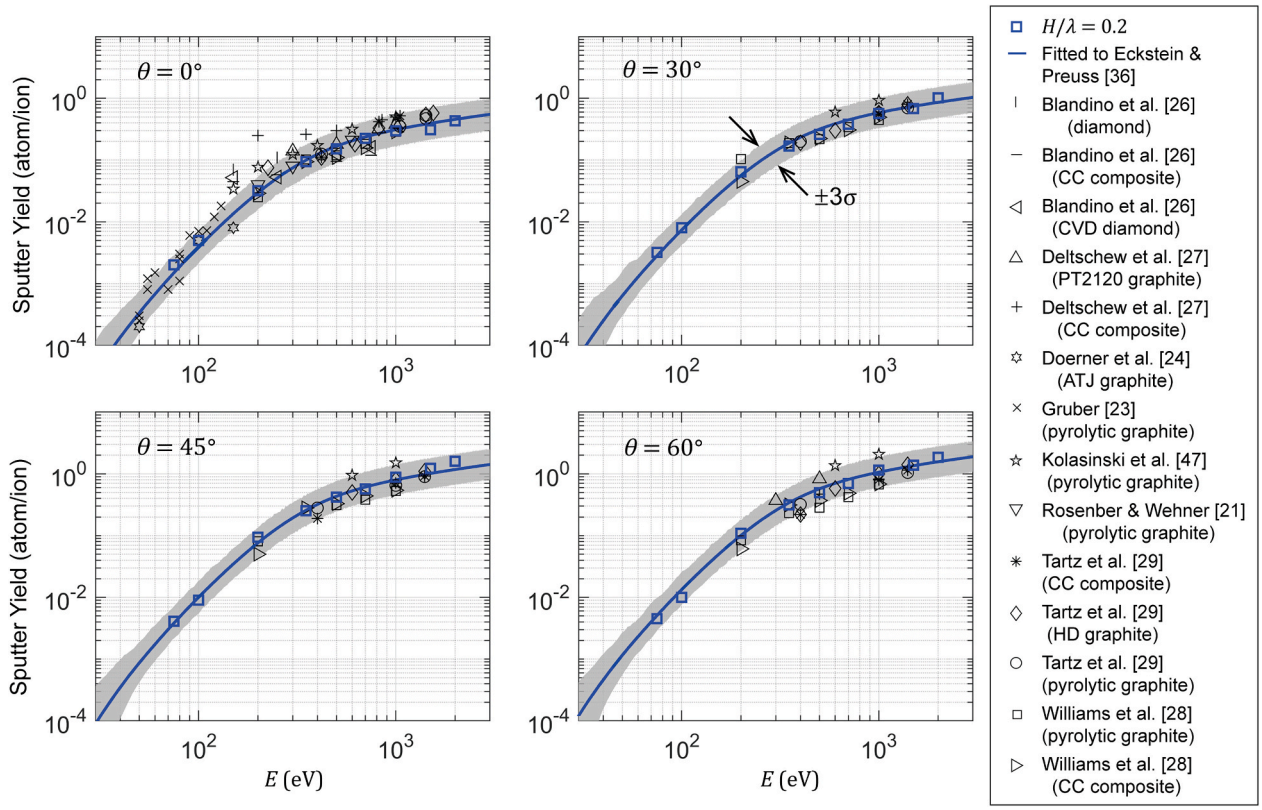

Fig. 10. Steady-state sputtering yield from MD simulations augmented to account for surface morphology effects ($\frac{H}{\lambda} = 0.2$; blue symbols) versus experiments for different carbon structures (black symbols). Solid blue lines denote maximum likelihood predictions of the Eckstein & Preuss [36] sputter yield model fitted to the MD results at $\frac{H}{\lambda} = 0.2$ (blue symbols), with the shaded grey region depicting the likelihood bounds of $\pm 3\sigma$, where σ is the standard deviation.

Table 1
Fitting parameters for the Eckstein & Preuss [36] sputter yield formula based on MD-derived data.

Parameters	Surface Morphology, H/λ				Experiment [60]
	0 (MD)	0.1	0.2	0.3	
Q (eV^{-1})	2.64	3.04	3.48	4.00	4
λ	3.96	3.80	4.01	3.86	0.8
μ	2.08	2.01	1.93	1.71	1.8
E_{th} (eV)	11.2	11.9	12.5	13.8	21
f	6.42	6.03	3.66	1.98	–
c	2.17	2.21	1.25	0.57	–
b	0.77	0.71	0.50	0.72	–

several orders of magnitude at lower ion energies of $\leq$ 300 eV. Studies have also fitted these semi-analytical formulas to experimental sputtering yields on carbon under low ion energies [47,60]. However, the experimental data for several polymorphs of carbon (black symbols in Fig. 6) shows a large spread between measurements conducted in different laboratories [24,26,27,29]. In addition, there is also no obvious correlation between the sputter yield data and the various polymorphs of carbon, including graphite, diamond, and carbon composites [26–29]. This is counterintuitive, in view of the large differences in sp^3 (711 kJ/mol) versus sp^2 (524 kJ/mol) bond strengths, coupled with the anisotropy character of the various forms and orientations of graphite caused by the relatively weak bonding between hexagonal planes of atoms [47]. In fact, Tartz et al. [29] found no appreciable differences between the sputtering yield measurements of carbon-carbon, pyrolytic graphite, and high-density graphite of various grain sizes, with xenon ion energies ranging between 400 eV and 1.4 keV. Similarly, William et al. [28] reported nearly identical differential and total sputter yield measurements of carbon-carbon composite and pyrolytic graphite across 200 eV $\leq E \leq$ 1 keV and 0° $\leq \theta \leq$ 60°.

Through MD simulations on the xenon ion bombardment of h-MLG, v-MLG, and diamond, we show that the bombardment process creates the same amorphous subsurface for each of these carbon structures once steady-state sputtering is achieved. Each of these amorphous subsurface structures possess similar atomic densities (porosities) and proportions of $sp/sp^2/sp^3$ bond types, and hence are virtually indistinguishable from one another. Their structural characteristics also remain unchanged with further ion bombardment. This explains why the sputtering yield under steady-state bombardment is independent of the initial carbon structure reported in experiments [28,29]. Furthermore, our simulations show that the same unique amorphous subsurface structure is attained under different ion energies and incidence angles, implying that the sputtering measurements at steady-state are also independent of the prior sputtering history. Ultimately, these results suggest that our steady-state sputtering measurements from MD are applicable to a wide array of carbon structures subjected to sputter erosion. In the application of electric space propulsion, this includes pyrolytic graphite used for gridded ion optics, diamond films for coatings of ion thruster electrodes, isotropic graphite for pole covers of Hall effect thrusters, and poco or anisotropic graphite used to line the panels of ground-based testing facilities of ion thrusters [14,19,20,61].

Performing large-scale atomistic simulations to account for micro-scale surface morphology effects is challenging because of the disparate length-scales. Instead, we idealize the surface geometry and consider changes to the sputtering yield (obtained from MD) caused by (a) changes to the local ion incidence angle at each impact point along the surface, (b) redeposition of sputterants which impact with surface features, as well as (c) partial shielding of the surface from incoming ions by surface features leading to a shadowing or masking effect. By augmenting the MD predictions to account for surface morphology effects of amorphous carbon films, our sputter yield predictions are well within

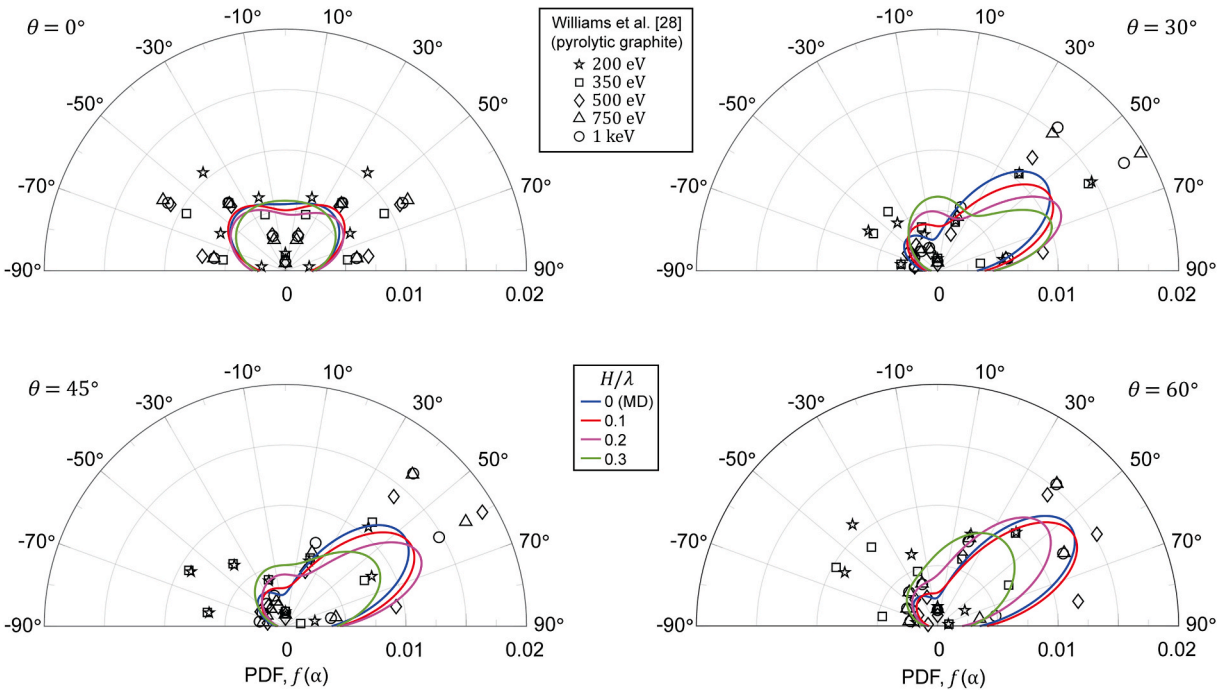

Fig. 11. Changes in the PDF of the differential yield profile of the sputterants, $f(\alpha)$, for different $\frac{H}{\lambda}$ at $\theta = 0°$, 30°, 45° and 60°. Open black symbols denote the experimentally-measured probability distribution with a bin size of $\pm$ 10° for five different ion energies [28].

the experimental scatter across the range of ion energies and incidence angles (Fig. 10). This allows us to calibrate semi-empirical sputter yield models with MD data for the first time, which is especially critical at lower ion energies because of the large scatter in experimental data caused by low sputter yields. Building on the high accuracy of our MD sputtering yield predictions, we further obtain differential yield profiles of the sputterants, which are necessary for quantifying the contribution of facility effects associated with carbon backsputtering. This differential yield data from MD complements the extremely limited set of experimental data available in the literature, which are highly non-trivial to obtain [19,31,62].

Surface morphology effects have been proposed to explain the differing sputtering yield data by Deltschew et al. [27] versus Williams et al. [28] and Tartz et al. [29] on carbon-carbon composites. While Deltschew et al. [27] demonstrated a two-fold higher sputtering yield for carbon-carbon composite compared to graphite, Williams et al. [28] and Tartz et al. [29] reported very similar sputtering yields between these two carbon structures – a conclusion more in line with our MD results. Unlike the carbon composite targets used by Williams et al. [28], however, the composite material characterized by Deltschew et al. [27] was not infiltrated with carbon or pyrolytically coated, and consequently, the carbon fibers were directly exposed to the ion beam. Thus, it was assumed by Williams et al. [28] that the exceptionally higher sputter yield for the carbon composite targets by Deltschew et al. [27] was due to the cylindrical fiber morphology (Fig. 12a and b – configuration 1). We show in Fig. 12c, however, that the sputtering yield caused by this cylindrical fiber morphology (blue dashed line), obtained by modifying (3) to account for the surface morphology in Fig. 12b – configuration 1, is not too different from that associated with a cosine surface morphology defined by $\frac{H}{\lambda} = 0.2$ (purple solid curve) which we have assumed for the various carbon polymorphs. However, Deltschew et al. [27] showed that the surface morphology of these carbon fibers also evolves with ion fluence (Fig. 12a). By idealizing these evolving surface geometries in Fig. 12b and modifying equations (2) and (3) accordingly, we show that the evolving sputter yield predictions transcending through these surface configurations appear to agree quantitatively with the experimental data of Deltschew et al. [27], at least for the higher ion energy values ($E \geq 500$ eV). We remark that at lower ion energies, the evolving surface morphology can be very different from those reproduced in Fig. 12a for $E = 500$ eV.

Our above analysis suggests the importance of accounting for the evolving surface morphology with ion fluence. Certainly, the surface features will change with the removal or redeposition of carbon sputterants, especially under high fluence (Fig. 12a). In addition, our MD simulations show that the energy of the carbon sputterants can range from 5 to 40 eV for $E = 200$ eV and as high as 25–200 eV for $E = 2$ keV (see sputterant energy distributions in Fig. S6 of the Supplementary Materials); the impact of the higher energy carbon sputterants on surface features can initiate further sputtering. In addition, the surface morphology may be affected by the entrapment of xenon ions within the subsurface, as quantified by the xenon ion absorption rate (Fig. S3 of the Supplementary Materials). Surface roughening caused by these effects may in turn be offset by smoothening due to surface diffusion operative at longer time-scales [56,63]. Accounting for all these complexities will require Monte Carlo simulations, and is a subject of future work.

5. Conclusion

Large-scale, massively-parallel MD simulations were conducted to elucidate the sputtering yield of carbon substrates across the range of ion energies and incidence angles of relevance to surface erosion in ion thrusters for electric space propulsion. Our extensive simulation data complements the sparse experimental datasets of carbon sputtering yield and differential yield profile, in an ion energy regime (< 1 keV) where obtaining statistically-accurate sputtering measurements becomes challenging in view of the very low carbon sputter rates. Our simulations uncovered the fundamental mechanism underpinning similar differential yield profiles and sputtering yields associated with different carbon target materials reported in experiments. We show that the bombardment of low energy heavy xenon ions creates an amorphous subsurface which, under steady-state conditions, possess the same structural characteristics (atomic density, $sp/sp^2/sp^3$ bond proportion) regardless of the initial carbon structure or the prior sputtering conditions. By upscaling our MD predictions to account for surface

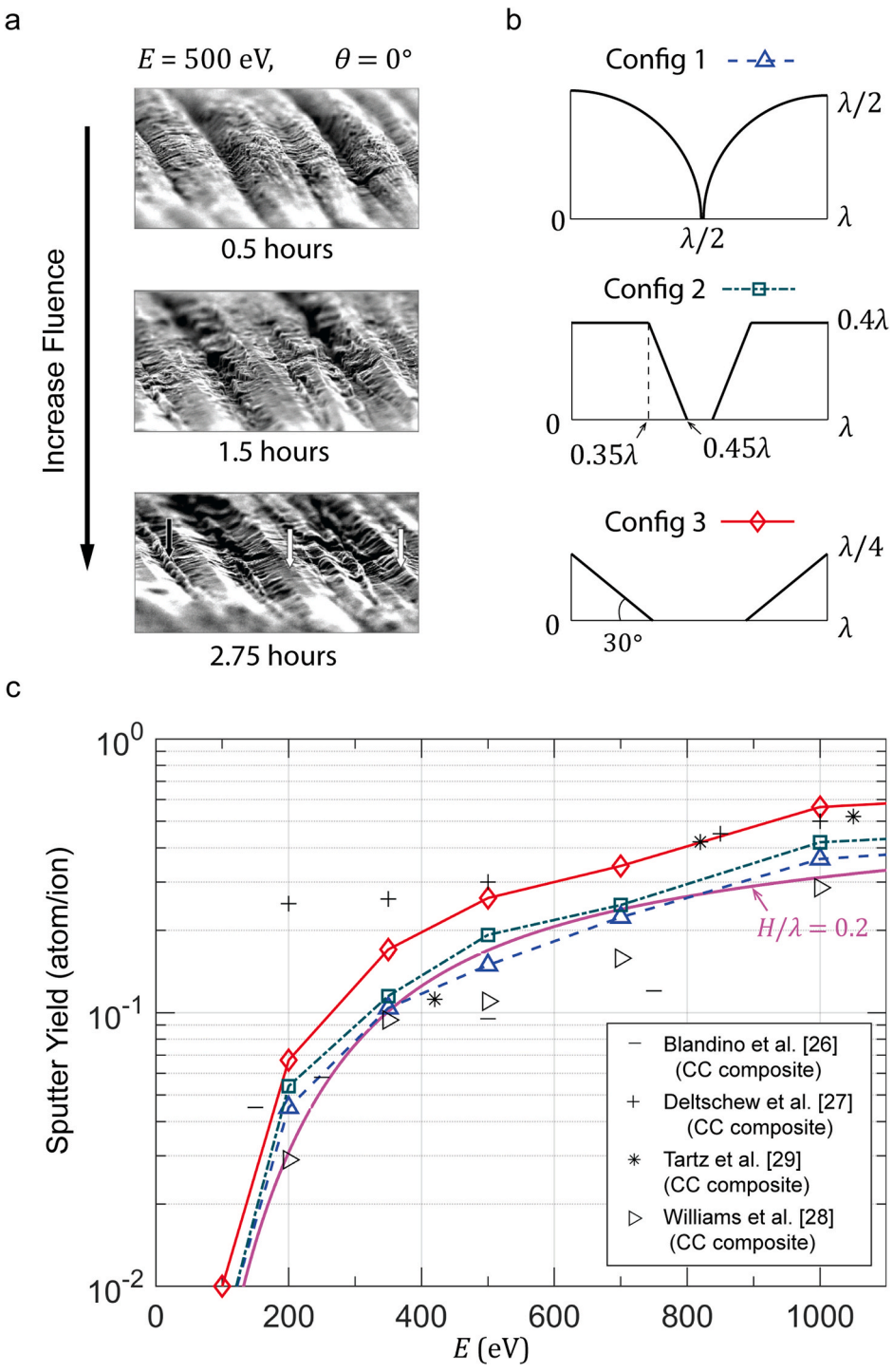

Fig. 12. (**a**) SEM imaging of the evolving surface morphology of the exposed carbon fiber under xenon ion bombardment with $E = 500$ eV and $\theta = 0°$ [27]. (**b**) Idealization of the evolving surface morphology in (**a**). (**c**) Steady-state sputtering yield across different E with $\theta = 0°$, comparing experiments for Carbon–Carbon composites with MD predictions based on the varying surface configurations in (**b**). Purple line denotes the maximum likelihood predictions of the Eckstein & Preuss [36] sputter yield model at $\frac{H}{\lambda} = 0.2$ (Fig. 11).

morphology effects, our sputter yield predictions were well within the experimental scatter, and could quantitatively explain the contrasting experimental results associated with the unique and evolving surface morphology of exposed carbon fibers. Parameters of a semi-empirical sputter-yield model were calibrated using this MD dataset, to provide a reduced order representation of the sputtering yield for plasma-surface interactions.

Authors' contributions

HT: carried out the numerical studies, conceived of the study, Formal analysis, participated in the analysis of the results, Writing – original draft, and wrote the paper. HBC: Supervision, supervised the research, conceived of the study, Formal analysis, participated in the analysis of the results, Writing – original draft, and wrote the paper.

Declaration of competing interest

The authors declare that they have no known competing financial interests or personal relationships that could have appeared to influence the work reported in this paper.

Acknowledgement

This work is supported by NASA through the Joint Advanced Propulsion Institute, a NASA Space Technology Research Institute, under grant number 80NSSC21K1118. We acknowledge the use of computational resources under the Delta research computing project, which is supported by the National Science Foundation (award OCI 2005572), and the State of Illinois. Delta is a joint effort of the University of Illinois at Urbana-Champaign and its National Center for Supercomputing Applications. The use of the Advanced Cyberinfrastructure Coordination Ecosystem: Services & Support (ACCESS), through allocations TG-PHY220010, TG-MAT210010, TG-MAT210031, and MSS22006 is also gratefully acknowledged.

Appendix A. Supplementary data

Supplementary data to this article can be found online at https://doi.org/10.1016/j.carbon.2023.01.015.

References

[1] E. Taglauer, Surface cleaning using sputtering, Appl. Phys. A 51 (3) (1990) 238–251, https://doi.org/10.1007/BF00324008.
[2] T. Šikola, L. Dittrichová, J. Spousta, J. Zlámal, J. Štefka, Cleaning of metal surfaces by a broad beam ion source, Nucl. Instrum. Methods Phys. Res. Sect. B Beam Interact. Mater. Atoms 127–128 (1997) 865–868, https://doi.org/10.1016/S0168-583X(97)00022-0.
[3] S.-P. Kim, H.B. Chew, E. Chason, V.B. Shenoy, K.-S. Kim, Nanoscale mechanisms of surface stress and morphology evolution in FCC metals under noble-gas ion bombardments, Proc. Math. Phys. Eng. Sci. 468 (2145) (2012) 2550–2573, https://doi.org/10.1098/rspa.2012.0042.
[4] L. Xie, L. Jiao, H. Dai, Selective etching of graphene edges by hydrogen plasma, J. Am. Chem. Soc. 132 (42) (2010) 14751–14753, https://doi.org/10.1021/ja107071g.
[5] M. Dvorak, W. Oswald, Z. Wu, Bandgap opening by patterning graphene, Sci. Rep. 3 (1) (2013), https://doi.org/10.1038/srep02289. Article 1.
[6] A. Davydova, E. Despiau-Pujo, G. Cunge, D.B. Graves, Etching mechanisms of graphene nanoribbons in downstream H2 plasmas: insights from molecular dynamics simulations, J. Phys. Appl. Phys. 48 (19) (2015), 195202, https://doi.org/10.1088/0022-3727/48/19/195202.
[7] A. Harpale, M. Panesi, H.B. Chew, Plasma-graphene interaction and its effects on nanoscale patterning, Phys. Rev. B 93 (3) (2016), 035416, https://doi.org/10.1103/PhysRevB.93.035416.
[8] A. Harpale, H.B. Chew, Hydrogen-plasma patterning of multilayer graphene: mechanisms and modeling, Carbon 117 (2017) 82–91, https://doi.org/10.1016/j.carbon.2017.02.062.
[9] H.C. Shih, C.P. Sung, W.L. Fan, C.K. Lee, Formation and tribological application of CVD diamond films on steels, Surf. Coating. Technol. 57 (2) (1993) 197–202, https://doi.org/10.1016/0257-8972(93)90040-U.
[10] W.L. Chan, E. Chason, Making waves: kinetic processes controlling surface evolution during low energy ion sputtering, J. Appl. Phys. 101 (12) (2007), 121301, https://doi.org/10.1063/1.2749198.
[11] Sk F. Ahmed, G.-H. Rho, J.Y. Lee, S.J. Kim, H.-Y. Kim, Y.-J. Jang, M.-W. Moon, K.-R. Lee, Nano-embossed structure on polypropylene induced by low energy Ar ion beam irradiation, Surf. Coating. Technol. 205 (2010) S104–S108, https://doi.org/10.1016/j.surfcoat.2010.06.005.
[12] S.H. Din, N.A. Sheikh, M.M. Butt, Mechanical and tribological behavior of microcrystalline CVD diamond coatings, J. Bio- Tribo-Corrosion 4 (2) (2018) 27, https://doi.org/10.1007/s40735-018-0144-1.
[13] J.N. Brooks, J.P. Allain, D.G. Whyte, R. Ochoukov, B. Lipschultz, Analysis of C-MOD molybdenum divertor erosion and code/data comparison, J. Nucl. Mater. 415 (1) (2011) S112–S116, https://doi.org/10.1016/j.jnucmat.2010.08.061.
[14] D.M. Goebel, B. Jorns, R.R. Hofer, I.G. Mikellides, I. Katz, Pole-Piece interactions with the plasma in a magnetically shielded Hall thruster, in: 50th AIAA/ASME/SAE/ASEE Joint Propulsion Conference, American Institute of Aeronautics and Astronautics, 2014, https://doi.org/10.2514/6.2014-3899.
[15] A. Hakola, J. Likonen, A. Lahtinen, T. Vuoriheimo, M. Groth, H. Kumpulainen, M. Balden, K. Krieger, M. Mayer, T. Schwarz-Selinger, S. Brezinsek, M. Kelemen, S. Markelj, M. Barac, S. Gouasmia, I.B. Radovic, A. Uccello, E. Vassallo, D. Dellasega, Contributors, the Euro. W. P., Gross and net erosion balance of plasma-facing materials in full-W tokamaks, Nucl. Fusion 61 (11) (2021), 116006, https://doi.org/10.1088/1741-4326/ac22d2.
[16] M. Tartz, E. Hartmann, R. Deltschew, H. Neumann, Experimental validation of a grid erosion simulation, in: 35th Joint Propulsion Conference and Exhibit, American Institute of Aeronautics and Astronautics, 1999, https://doi.org/10.2514/6.1999-2860.
[17] M. Patterson, M. Domonkos, J. Foster, T. Haag, L. Pinero, G. Soulas, Ion propulsion development activities at the NASA glenn research center, in: 39th AIAA/ASME/SAE/ASEE Joint Propulsion Conference and Exhibit, American Institute of Aeronautics and Astronautics, 2003, https://doi.org/10.2514/6.2003-4709.
[18] R.B. Lobbia, J.E. Polk, R.R. Hofer, V.H. Chaplin, B. Jorns, Accelerating 23,000 hours of ground test backsputtered carbon on a magnetically shielded Hall thruster, in: AIAA Propulsion and Energy 2019 Forum, American Institute of Aeronautics and Astronautics, 2019, https://doi.org/10.2514/6.2019-3898.
[19] G. Williams, T. Haag, J. Foster, J.V. Noord, S. Malone, T. Hickman, M. Patterson, Analysis of the pyrolytic graphite ion optics following the 2000-hour wear test of the HiPEP ion thruster, in: 42nd AIAA/ASME/SAE/ASEE Joint Propulsion Conference & Exhibit, American Institute of Aeronautics and Astronautics, 2006, https://doi.org/10.2514/6.2006-5005.
[20] G.C. Soulas, The impact of back-sputtered carbon on the accelerator grid wear rates of the NEXT and NSTAR ion thrusters, in: International Electric Propulsion Conference, 2013, October 6. Washington, D.C, https://ntrs.nasa.gov/citations/20150021367.
[21] D. Rosenberg, G.K. Wehner, Sputtering yields for low energy He + -, Kr + -, and Xe + -ion bombardment, J. Appl. Phys. 33 (5) (1962) 1842–1845, https://doi.org/10.1063/1.1728843.
[22] E. Hechtl, J. Bohdansky, Sputtering behavior of graphite and molybdenum at low bombarding energies, J. Nucl. Mater. 123 (1–3) (1984) 1431–1436, https://doi.org/10.1016/0022-3115(84)90280-0.
[23] J. Gruber, Low-Energy Sputter Erosion of Various Materials in a T 5. 27th International Electric Propulsion Conference, 2001.
[24] R.P. Doerner, D.G. Whyte, D.M. Goebel, Sputtering yield measurements during low energy xenon plasma bombardment, J. Appl. Phys. 93 (9) (2003) 5816–5823, https://doi.org/10.1063/1.1566474.
[25] E. Oyarzabal, R.P. Doerner, M. Shimada, G.R. Tynan, Carbon atom and cluster sputtering under low-energy noble gas plasma bombardment, J. Appl. Phys. 104 (4) (2008), 043305, https://doi.org/10.1063/1.2968549.
[26] J.J. Blandino, D.G. Goodwin, C.E. Garner, Low energy sputter yields for diamond, carbon–carbon composite, and molybdenum subject to xenon ion bombardment, Diam. Relat. Mater. 9 (12) (2000) 1992–2001, https://doi.org/10.1016/S0925-9635(00)00350-2.
[27] R. Deltschew, M. Tartz, V. Plicht, E. Hartmann, H. Neumann, Sputter Characteristics of Carbon-Carbon Compound Material. 27th International Electric Propulsion Conference, 2001.
[28] J. Williams, M. Johnson, D. Williams, Differential Sputtering Behavior of Pyrolytic Graphite and Carbon-Carbon Composite under Xenon Bombardment, 40th AIAA/ASME/SAE/ASEE Joint Propulsion Conference and Exhibit, Fort Lauderdale, Florida, 2004, https://doi.org/10.2514/6.2004-3788.
[29] M. Tartz, H. Neumann, H. Leiter, J. Esch, Pyrolytic graphite and carbon-carbon sputter behaviour under xenon ion incidence, in: 29th International Electric Propulsion Conference, 10, 2005.
[30] S. Habenicht, Morphology of graphite surfaces after ion-beam erosion, Phys. Rev. B 63 (12) (2001), 125419, https://doi.org/10.1103/PhysRevB.63.125419.
[31] A.P. Yalin, J.D. Williams, V. Surla, K.A. Zoerb, Differential sputter yield profiles of molybdenum due to bombardment by low energy xenon ions at normal and oblique incidence, J. Phys. Appl. Phys. 40 (10) (2007) 3194, https://doi.org/10.1088/0022-3727/40/10/025.
[32] Q. Wei, K.-D. Li, J. Lian, L. Wang, Angular dependence of sputtering yield of amorphous and polycrystalline materials, J. Phys. Appl. Phys. 41 (17) (2008), 172002, https://doi.org/10.1088/0022-3727/41/17/172002.
[33] P. Sigmund, Sputtering by ion bombardment theoretical concepts, in: R. Behrisch (Ed.), Sputtering by Particle Bombardment I, Springer Berlin Heidelberg, 1981, pp. 9–71, https://doi.org/10.1007/3540105212_7, 47.
[34] J. Bohdansky, A universal relation for the sputtering yield of monatomic solids at normal ion incidence, Nucl. Instrum. Methods Phys. Res. Sect. B Beam Interact. Mater. Atoms 2 (1) (1984) 587–591, https://doi.org/10.1016/0168-583X(84)90271-4.
[35] Y. Yamamura, S. Shindo, An empirical formula for angular dependence of sputtering yields, Radiat. Eff. 80 (1–2) (1984) 57–72, https://doi.org/10.1080/00337578408222489.
[36] W. Eckstein, R. Preuss, New fit formulae for the sputtering yield, J. Nucl. Mater. 320 (3) (2003) 209–213, https://doi.org/10.1016/S0022-3115(03)00192-2.
[37] J.F. Ziegler, The stopping of energetic ions in solids, Nucl. Instrum. Methods 168 (1) (1980) 17–24, https://doi.org/10.1016/0029-554X(80)91225-2.
[38] J.W. Wilson, F.A. Cucinotta, H. Tai, J.L. Shinn, S.Y. Chun, R.K. Tripathi, L. Sihver, Transport of light ions in matter, Adv. Space Res. 21 (12) (1998) 1763–1771, https://doi.org/10.1016/S0273-1177(98)00063-5.
[39] J.F. Ziegler, M.D. Ziegler, J.P. Biersack, Srim – the stopping and range of ions in matter (2010), Nucl. Instrum. Methods Phys. Res. Sect. B Beam Interact. Mater. Atoms 268 (11) (2010) 1818–1823, https://doi.org/10.1016/j.nimb.2010.02.091.
[40] M. Titze, J.L. Pacheco, T. Byers, S.B. Van Deusen, D.L. Perry, D. Weathers, E. S. Bielejec, Evaluation of the accuracy of stopping and range of ions in matter simulations through secondary ion mass spectrometry and Rutherford backscattering spectrometry for low energy heavy ion implantation, J. Vac. Sci. Technol. 39 (6) (2021), https://doi.org/10.1116/6.0001406. Article SAND-2021-13560J.
[41] A.P. Thompson, H.M. Aktulga, R. Berger, D.S. Bolintineanu, W.M. Brown, P. S. Crozier, P.J. 't Veld, A. Kohlmeyer, S.G. Moore, T.D. Nguyen, R. Shan, M. J. Stevens, J. Tranchida, C. Trott, S.J. Plimpton, Lammps - a flexible simulation tool for particle-based materials modeling at the atomic, meso, and continuum scales, Comput. Phys. Commun. 271 (2022), 108171, https://doi.org/10.1016/j.cpc.2021.108171.
[42] S.J. Stuart, A.B. Tutein, J.A. Harrison, A reactive potential for hydrocarbons with intermolecular interactions, J. Chem. Phys. 112 (14) (2000) 6472–6486, https://doi.org/10.1063/1.481208.

[43] C. Qian, B. McLean, D. Hedman, F. Ding, A comprehensive assessment of empirical potentials for carbon materials, Apl. Mater. 9 (6) (2021), 061102, https://doi.org/10.1063/5.0052870.
[44] M. Wen, E.B. Tadmor, Hybrid neural network potential for multilayer graphene, Phys. Rev. B 100 (19) (2019), 195419, https://doi.org/10.1103/PhysRevB.100.195419.
[45] J.F. Ziegler, J.P. Biersack, The stopping and range of ions in matter, in: D. A. Bromley (Ed.), Treatise on Heavy-Ion Science: Volume 6: Astrophysics, Chemistry, and Condensed Matter, Springer US, 1985, pp. 93–129, https://doi.org/10.1007/978-1-4615-8103-1_3.
[46] M.S. Daw, M.I. Baskes, Embedded-atom method: derivation and application to impurities, surfaces, and other defects in metals, Phys. Rev. B 29 (12) (1984) 6443–6453, https://doi.org/10.1103/PhysRevB.29.6443.
[47] R.D. Kolasinski, J. Polk, D. Goebel, L. Johnson, Carbon sputtering yield measurements at grazing incidence, in: 42nd AIAA/ASME/SAE/ASEE Joint Propulsion Conference & Exhibit, 2006, https://doi.org/10.2514/6.2006-4337. Sacramento, California.
[48] R.D. Kolasinski, J.E. Polk, D. Goebel, L.K. Johnson, Sputtering yield measurements at glancing incidence using a quartz crystal microbalance, J. Vac. Sci. Technol. 25 (2) (2007) 236–245, https://doi.org/10.1116/1.2435375.
[49] H. Edelsbrunner, E.P. Mücke, Three-dimensional alpha shapes, ACM Trans. Graph. 13 (1) (1994) 43–72, https://doi.org/10.1145/174462.156635.
[50] W.D. Wilson, L.G. Haggmark, J.P. Biersack, Calculations of nuclear stopping, ranges, and straggling in the low-energy region, Phys. Rev. B 15 (5) (1977) 2458–2468, https://doi.org/10.1103/PhysRevB.15.2458.
[51] J. Bohdansky, Important sputtering yield data for tokamaks: a comparison of measurements and estimates, J. Nucl. Mater. 93 (94) (1980) 44–60, https://doi.org/10.1016/0022-3115(80)90302-5.
[52] M.J. Pellin, R.B. Wright, D.M. Gruen, Laser fluorescence spectroscopy of sputtered zirconium atoms, J. Chem. Phys. 74 (11) (1981) 6448–6457, https://doi.org/10.1063/1.440983.
[53] S. Hadrath, J. Ehlbeck, G. Lieder, F. Sigeneger, Determination of absolute population densities of eroded tungsten in hollow cathode lamps and fluorescent lamps by laser-induced fluorescence, J. Phys. Appl. Phys. 38 (17) (2005) 3285, https://doi.org/10.1088/0022-3727/38/17/S33.
[54] C.E. Huerta, T.S. Matlock, R.E. Wirz, View factor modeling of sputter-deposition on micron-scale-architectured surfaces exposed to plasma, J. Appl. Phys. 119 (11) (2016), 113303, https://doi.org/10.1063/1.4944035.
[55] M.J. Schaible, C.A. Dukes, A.C. Hutcherson, P. Lee, M.R. Collier, R.E. Johnson, Solar wind sputtering rates of small bodies and ion mass spectrometry detection of secondary ions, J. Geophys. Res.: Planets 122 (10) (2017) 1968–1983, https://doi.org/10.1002/2017JE005359.
[56] R.M. Bradley, J.M.E. Harper, Theory of ripple topography induced by ion bombardment, J. Vac. Sci. Technol. 6 (4) (1988) 2390–2395, https://doi.org/10.1116/1.575561.
[57] S. Habenicht, Nanometer ripple formation and self-affine roughening of ion-beam-eroded graphite surfaces, Phys. Rev. B 60 (4) (1999) R2200–R2203, https://doi.org/10.1103/PhysRevB.60.R2200.
[58] C. García-Rosales, W. Eckstein, J. Roth, Revised formulae for sputtering data, J. Nucl. Mater. 218 (1) (1995) 8–17, https://doi.org/10.1016/0022-3115(94)00376-9.
[59] R.C. Smith, Uncertainty Quantification: Theory, Implementation, and Applications, Society for Industrial and Applied Mathematics, 2013.
[60] J.T. Yim, A survey of xenon ion sputter yield data and fits relevant to electric propulsion spacecraft integration, in: 35th International Electric Propulsion Conference, 2017.
[61] P.M. Sforza, Chapter 14—space propulsion, in: P.M. Sforza (Ed.), Theory of Aerospace Propulsion, Butterworth-Heinemann, 2012, pp. 541–565, https://doi.org/10.1016/B978-1-85617-912-6.00014-1.
[62] G.Z. Li, T.S. Matlock, D.M. Goebel, C.A. Dodson, C.S.R. Matthes, N.M. Ghoniem, R. E. Wirz, In situ plasma sputtering and angular distribution measurements for structured molybdenum surfaces, Plasma Sources Sci. Technol. 26 (6) (2017), 065002, https://doi.org/10.1088/1361-6595/aa6a7d.
[63] R.L. Headrick, H. Zhou, Ripple formation and smoothening on insulating surfaces, J. Phys. Condens. Matter: Inst. Phys. J. 21 (22) (2009), 224005, https://doi.org/10.1088/0953-8984/21/22/224005.